

30 m global impervious surface area dynamics and urban expansion pattern observed by Landsat satellites: From 1972 to 2019

Xin HUANG^{1,2}, Jiayi LI^{1*}, Jie YANG¹, Zhen ZHANG¹, Dongrui LI¹ & Xiaoping LIU³

¹ School of Remote Sensing and Information Engineering, Wuhan University, Wuhan 430079, China;

² State Key Laboratory of Information Engineering in Surveying, Mapping and Remote Sensing, Wuhan University, Wuhan 430079, China;

³ Guangdong Key Laboratory for Urbanization and Geo-simulation, School of Geography and Planning, Sun Yat-Sen University, Guangzhou 510006, China

Received November 5, 2020; revised April 12, 2021; accepted May 25, 2021; published online July 26, 2021

Abstract Using more than three million Landsat satellite images, this research developed the first global impervious surface area (GISA) dataset from 1972 to 2019. Based on 120,777 independent and random reference sites from 270 cities all over the world, the omission error, commission error, and F-score of GISA are 5.16%, 0.82%, and 0.954, respectively. Compared to the existing global datasets, the merits of GISA include: (1) It provided the global ISA maps before the year of 1985, and showed the longest time span (1972–2019) and the highest accuracy (in terms of a large number of randomly selected and third-party validation sample sets); (2) it presented a new global ISA mapping method including a semi-automatic global sample collection, a locally adaptive classification strategy, and a spatio-temporal post-processing procedure; and (3) it extracted ISA from the whole global land area (not from an urban mask) and hence reduced the underestimation. Moreover, on the basis of GISA, the long time series global urban expansion pattern (GUEP) has been calculated for the first time, and the pattern of continents and representative countries were analyzed. The two new datasets (GISA and GUEP) produced in this study can contribute to further understanding on the human's utilization and reformation to nature during the past half century, and can be freely download from <http://irsip.whu.edu.cn/resources/dataweb.php>.

Keywords Landsat, Urban, Google earth engine, Impervious area, Urban expansion

Citation: Huang X, Li J, Yang J, Zhang Z, Li D, Liu X. 2021. 30 m global impervious surface area dynamics and urban expansion pattern observed by Landsat satellites: From 1972 to 2019. *Science China Earth Sciences*, 64(11): 1922–1933, <https://doi.org/10.1007/s11430-020-9797-9>

1. Introduction

For half a century, human's activities drastically altered the climate, environment, and ecosystem of the Earth, which restricted the sustainable development and affected the human well-being (Mbow et al., 2017; Kuang, 2019). Impervious surface areas (ISA), i.e., artificial structures with impermeable characteristics, mainly including roofs, paved surfaces, roads, and hardened grounds, are the most affected

regions. The dynamic of ISA is a critical indicator for understanding the urban land change and assessing the influence of human on nature (Seto et al., 2012). Since ISA expansion can prevent rainwater from seeping, block surface evapotranspiration (Krayenhoff et al., 2018), increase surface runoff (Weng, 2001), and affect the biodiversity and ecosystem services (Seto et al., 2012), many global organizations have paid increasing attention to monitoring ISA dynamics. For examples, in addition to a new chapter concerning the urban mitigation of climate change in Inter-governmental Panel on Climate Change (IPCC) Fifth

* Corresponding author (email: zjjerica@whu.edu.cn)

Assessment Reports (Seto et al., 2014), its Seventh Reports further approved a Special Report on Cities and Climate Change (IPCC, 2016). Moreover, the United Nations (UN) Convention on Biodiversity Cities and Biodiversity Outlook emphasized the critical role of urban land expansion in altering ecosystem services and biodiversity (Campbell et al., 2012), and UN Sustainable Development Goal (SDG) also laid stress on urban land change (<https://sdg-tracker.org/cities>). Thus, a global ISA product documenting long time series change at fine spatio-temporal resolution is of great research significance.

Satellite remote sensing observations are primary data source for global ISA monitoring. With the progress of satellite image acquisition and interpretation technologies, the spatial-temporal granularity of the global products has been remarkably improved, e.g., from static to multi-temporal records, and from coarse (≥ 1 km) to fine (~ 30 m) spatial scales. For instance, the Joint Research Centre (JRC) of European Union comprehensively exploited SPOT-4 (Satellite Pour l'Observation de la Terre -4, spatial resolution: 1.15 km) images and compiled a harmonized global land cover classification for the year 2000 (GLC2000) (Bartholomé and Belward, 2005). Food and Agriculture Organization of the United Nations (FAO) combined multi-source medium-resolution satellite remote sensing data with a pixel resolution of 250–300 m to create a global land cover database (GLC-SHARE) (Latham et al., 2014) with spatial resolution of 30 arc-seconds for the year 2012. In recent years, European Space Agency (ESA) published two 300 m global archives (GlobCover for short) in the year of 2005 (Bicheron et al., 2006) and 2009 (Bontemps et al., 2011), as well as its improved version (CCI-LC for short) (ESA, 2017), based on 300 m Medium Resolution Imaging Spectrometer (MERIS), 1 km SPOT vegetation Proba-V, and 1 km Advanced Very High Resolution Radiometer (AVHRR) during 1992 and 2018. Meanwhile, National Aeronautics and Space Administration (NASA) released the annual global land cover products for 2001–2018 with spatial resolution of 250 m (Sulla-Menashe et al., 2019), on the basis of Moderate Resolution Imaging Spectroradiometer (MODIS) images. More recently, German Aerospace Center (DLR) produced the global built-up product with the finest resolution in the year of 2014 (GUF for short, spatial resolution: 12 m) (Esch et al., 2017), derived from $\sim 180,000$ TerraSAR-X/TanDEM-X remote sensing images. In summary, the advantages of the coarse-resolution products lie in their rich image sources, relatively light computational burden, frequent revisit, which are beneficial to the long time series dynamic monitoring and the intra-year phenological information characterization (Xu et al., 2020). However, the deficiencies of the coarse-resolution products lie in the omission of small-sized ISA (Sulla-Menashe et al., 2019) and the mixed pixel problems (Yang et al., 2017). On the other hand, the fine-resolution

products can delineate detailed land cover, but suffer from heavy computational cost (Schneider, 2012) and insufficiency of time-series information (Liu et al., 2019b). Notably, in recent years, with the application and development of cloud computing platforms (e.g., Google earth engine, GEE), the storage and computing capacity has been greatly improved, which signifies the arrival of the era of global mapping with high spatial resolution.

In this context, the Landsat satellites, which began to acquire images from 1972 with fine spatial resolution and frequent revisit, are the most appropriate platform for large-scale ISA monitoring (Ran and Li, 2015; Wulder et al., 2016; Gong et al., 2019). On the basis of Landsat images, the earliest global ISA product is Global Human Settlement Layer (GHSL) (Pesaresi et al., 2015), consisting of four periods with spatial resolution of 38 m: 1975, 1990, 2000 and 2014. Recently, Liu et al. (2020) produced an annual urban area dataset (called global annual urban dynamics, GAUD) with a resolution of 30 m from 1985 to 2015; meanwhile, Gong et al. (2020) produced global artificial impervious areas (GAIA), to quantify annual urban ISA dynamic from 1985 to 2018. More recently, JRC released a new version of GHSL, where a global ISA probability grid for year 2018 was reported (Corbane et al., 2020). Nevertheless, currently, although there have been several global 30 m ISA datasets available, the differences between these products exist, due to their distinct sample collection, classification, post-processing, and accuracy assessment methods, leading to large discrepancies in the global/regional ISA estimation. In particular, the current two 30 m global annual ISA datasets, GAIA and GAUD, do not provide the global ISA information before the year of 1985, owing to the Landsat data deficiency. Therefore, the long time-series and high spatio-temporal resolution global ISA mapping is still a great challenge, and it is worthwhile to further developing new technologies and products to improve the accuracy, expand the time span, and finally strengthen our knowledge on the global ISA dynamics. Therefore, the first objective of this study is to develop the global ISA dataset from 1972 to 2019 (GISA), using more than three million Landsat satellite images.

Furthermore, on the basis of GISA, we are able to analyze the time-series pattern of global urban expansion. The expansion pattern can reflect the spatio-temporal characteristics and change rules of urban growth, which is of great significance to urban management and planning. Previous works mainly focused on several developed cities (e.g., <https://www.c40.org/networks>), regional areas (Krayenhoff et al., 2018; Xu et al., 2019b), or countries (Schneider and Mertes, 2014; Huang et al., 2019; Li et al., 2020). However, as indicated by Reba and Seto (2020), current research ignored the small-medium cities and Global South, which are the fastest growing areas in the past decades and will be the urbanization hotspots for decades to come (United Nations, 2018). In addition, most of the current studies only used several cross-

section records (e.g., every five or ten years) to analyze the long-term urban expansion pattern (Schneider and Mertes, 2014; Krayenhoff et al., 2018; Xu et al., 2019b). Therefore, the existing urban expansion pattern analysis is not sufficient. In this context, the second objective of this research is to analyze the urban expansion in a high-frequency manner, based on our long-time series global ISA product.

2. Materials and methods

With the platform of Google Earth Engine (GEE), 30,872,690 Landsat images with less than 80% cloud cover from Jan 1972 to Nov 2019 were fed into a machine learning workflow to produce our GISA (global impervious surface area) dataset. Considering the spatiotemporal coverage of available Landsat archives (Appendix Figure S1, <https://link.springer.com>), the images acquired from 1972 to 1977, and 1978 to 1984 were combined to map the global ISA product at the first and second period, respectively, and since 1985, the annual product was generated using the Landsat images available. On the basis of the GISA maps, spatial pattern of global urban expansion are further analyzed.

2.1 Global ISA mapping

In general, we designed a distributed mapping framework (Figure 1): first, the global land surface was divided into 1221 hexagons with a side length of 2°, then, for each hexagon in each period, a random forest classifier locally trained with the obtained samples was used to classify the land surface into ISA and non-ISA. Finally, a spatio-temporal post-processing approach was conducted for the time-series global maps throughout the 48 years

For each hexagon, the mapping algorithm mainly consists of the following three blocks.

(1) Training sample generation. The ISA/non-ISA samples were picked from the overlapping regions of a set of existing global mapping products, and were further screened by a series of spectral-spatial-temporal rules. Please note that some of the obtained ISA sample sets were checked visually to ensure their quality. The technique details are provided in Appendix Text S1.

(2) Feature extraction and classification. For each hexagon in each mapping period, a random forest classifier was trained with the obtained samples, and the elevation and slope calculated from Digital Elevation Model (DEM) data and the time-series spectral characteristics from Landsat images were stacked as input feature. Considering the quality of DEM data, we used DEM data from Shuttle Radar Topographic Mission for regions with latitude above 58°N, and DEM data from Global Multi-resolution Terrain Elevation Data 2010 (GMTD2010) for regions with latitude below 58°N. The spectral characteristics included all the spectral reflectance and the normalized difference spectral indices (in their 20%, 50% and 80% percentiles) as well as their multi-temporal standard deviations, as suggested by related studies (Sulla-Menashe et al., 2019; Li et al., 2020).

(3) Post-processing. The night-time night data were first used to suppress the false alarms of ISA in the arid regions, and subsequently, a series of post-processing steps, including gap filling, spatio-temporal filtering, and time-series reasoning, were proposed to further refine the mapping results (see Appendix Text S2 for the post-processing technique details).

2.2 ISA mapping accuracy assessment

It is an extremely challenging task to assess the accuracy of global high-resolution ISA product in such a dense and large time span. In this study, we used three validation sets, including (1) a stratified randomly selected 120,777 sample set from 270

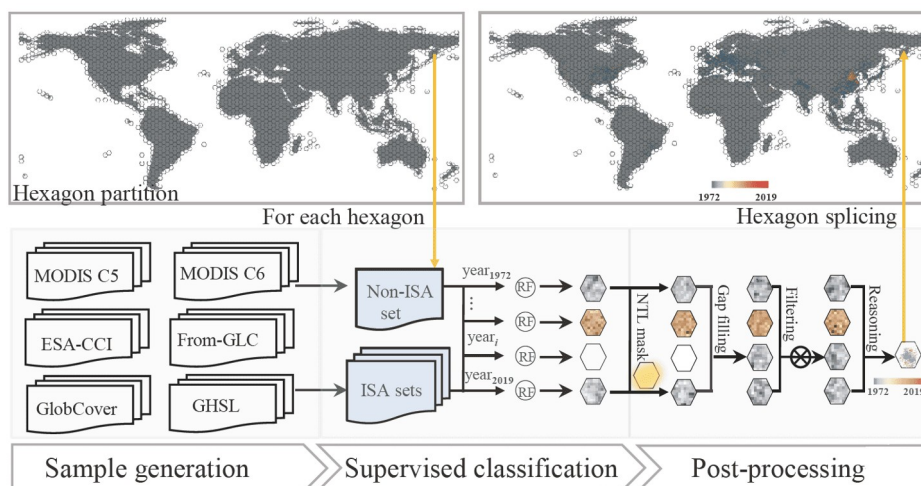


Figure 1 Flowchart of the global ISA mapping framework.

global cities, (2) 88,822 random samples selected from a high spatial resolution (2 m) built-up dataset over global 45 urban-suburban areas (Liu et al., 2019a), and (3) 56,703 settlement points in Global Rural-Urban Mapping Project (Balk et al., 2006). Please note that the time between the reference datasets and the corresponding GISA product is consistent.

(1) Stratified random sampling in 270 global cities. We randomly selected global ISA/non-ISA validation points for the year of 1972, 1978, 1985, 1990, 1995, 2000, 2005, 2010, 2015, and 2018. The selected points were interpreted in terms of the high-resolution images from Google™ Earth as well as Landsat images. The selection and interpretation of validation samples were independent to the ISA mapping. For each year, 27 cities across the world were randomly selected in terms of their population and biomes, including 7 cities with population larger than 5 million, 10 cities with population ranging from 1 to 5 million, and 10 cities with population smaller than 1 million. According to Olofsson et al. (2014), we collected 10,000–15,000 random points for each year, and the number of validation points in each city was proportional to its city area. In total, 120,777 validation points were generated. Omission error (OE), Commission error (CE), and F-score (harmonic mean of user accuracy and producer accuracy) of the ISA based on the 120,777 points were used to assess the accuracy of the ISA products. The spatial distribution of the 270 cities as well as their F-scores are provided in Appendix Figure S2.

(2) Validation on a high spatial resolution product of 45 global cities. A high spatial resolution product, based on the ZY-3 multi-view satellite images in 45 global cities covering both urban and suburban areas (Liu et al., 2019a), were also used to assess the accuracy of GISA product. The built-up areas extracted from ZY-3 images were adopted as a validation set since they have a relatively high spatial resolution (2 m) and meanwhile their multi-view imaging mode is effective in describing the vertical characteristics of urban structures. Specifically, an ISA sample point was chosen when more than 80% pixels in its 30 m×30 m neighbor are built-up pixels, and a non-ISA point was identified only when all the pixels in its 30 m×30 m neighbor are covered by natural lands. Similarly, for each city, the number of validation points is proportional to its urban area. Finally, each point was visually checked based on ZY-3 images. In this way, 9,477 ISA and 79,345 non-ISA points were generated.

(3) Validation on the Global Rural-Urban Mapping Project (GRUMP). In addition, we used the settlement points from GRUMP (Balk et al., 2006) to assess the ISA products. The evaluation method is the same as Gong et al. (2020), i.e. multi-scale buffers with diameters of 30, 100, 250, 500, and 1000 m were used to calculate the proportion of the ISA within each buffer zone, and a pixel is correctly identified as an ISA when more than 20% pixels in its buffer zone are covered by ISA. In this way, the accuracy of the ISA pro-

ducts can be assessed by counting the numbers of recognized points in a multi-scale manner, and more identified points signify better performance.

2.3 Urban expansion pattern analysis

2.3.1 Urban ISA extraction

In order to analyze the urban expansion pattern, according to Zhou et al. (2014), we first extract urban ISA from GISA map via the following steps:

Step 1. A built-up intensity map is calculated through a 1 km×1 km sliding window, and a 50% threshold is used to divide the intensity map into high- and low-intensity built-up land.

Step 2. To include the scattered but spatially adjacent high-intensity built-up parcels into the urban area, a buffer distance of 2 km is used to aggregate these parcels and form the boundary of urban area. Please note that the parameters, such as window size (1 km), threshold of built-up intensity (50%), and aggregation distance (2 km) are determined according to Zhou et al. (2014).

2.3.2 Urban expansion types

According to Camagni et al. (2002), there are three types of urban growth pattern: leap-frogging, infilling, and edge-expansion. The urban growth type (E) of a newly developed patch (P) was calculated by the following equation (Huang et al., 2019):

$$E = \frac{N_p}{C}, \quad (1)$$

where N_p is boundary length of P , C is common boundary length between P and the existing ISAs. The growth type is identified as leapfrogging when $E=0$, infilling when $E>0.5$, and edge-expansion when $0<E\leq 0.5$. Generally, the construction of new towns and the transformation from rural settlements to urban built-up are the main causes of leapfrogging patches. Infilling patches mainly correspond to the intensive utilization of urban land, and edge-expansion patches usually appear in the urban fringe areas, reflecting the urban sprawl.

Considering the shortage of valid observations for the Landsat images before 1985 (Appendix Figure S3), we calculated and analyzed the global urban expansion pattern since 1986. In addition, we calculated the expansion pattern every two years, considering the urban expansion rate and computational cost.

3. Results and discussions

3.1 Global impervious surface area (GISA) mapping

As seen from the right column of Table 1, using the vali-

Table 1 Accuracy comparison between existing global 30 m ISA products

ZY-3 high-resolution reference set				validation points based on 270 cities			
GAIA	ISA	non-ISA	Precision	GAIA	ISA	Non-ISA	Precision
ISA	29912	7237	80.52%	ISA	12765	638	95.24%
non-ISA	6033	69006	91.96%	Non-ISA	2640	77024	96.69%
Recall	83.22%	90.51%		Recall	82.86%	99.18%	
OE of ISA	16.78%	CE of ISA	19.48%	OE of ISA	17.14%	CE of ISA	4.76%
F-score of ISA	0.818	OA	88.17%	F-score of ISA	0.886	OA	96.48%
GAUD	ISA	non-ISA	Precision	GAUD	ISA	Non-ISA	Precision
ISA	29722	5389	84.65%	ISA	14339	820	94.59%
non-ISA	6223	70854	91.93%	Non-ISA	1132	76842	98.55%
Recall	82.69%	92.93%		Recall	92.68%	98.94%	
OE of ISA	17.31%	CE of ISA	15.35%	OE of ISA	7.32%	CE of ISA	5.41%
F-score of ISA	0.837	OA	89.65%	F-score of ISA	0.936	OA	97.90%
GISA	ISA	non-ISA	Precision	GISA	ISA	Non-ISA	Precision
ISA	30583	5081	85.75%	ISA	14734	314	97.91%
non-ISA	5362	71162	92.99%	Non-ISA	671	77348	99.14%
Recall	85.08%	93.34%		Recall	95.64%	99.60%	
OE of ISA	14.92%	CE of ISA	14.25%	OE of ISA	4.36%	CE of ISA	2.09%
F-score of ISA	0.854	OA	90.69%	F-score of ISA	0.968	OA	98.94%

dation points from the 270 cities, OE, CE and F-score of ISA is 5.16%, 0.82% and 0.954, respectively. Based on the high spatial resolution validation points from ZY-3 built-up product (see the left column of Table 1), these accuracy metrics are 14.12%, 14.25% and 0.854, respectively. It can be said that our developed GISA dataset shows desirable performance on both reference sets. In order to further show the superiority of our GISA dataset on the rural ISA mapping, the existing fine-resolution (30 m) global products in 1990 and 2015 are compared in Table 2. It can be seen that GISA reaches the highest F-score in both urban and rural regions. Moreover, the area of the rural ISA identified by GISA is also larger than GAIA and GAUD, which, to some extent, reflects a smaller omission of GISA.

According to GISA, the global ISA extent has been increased by 3.23–3.29 times in the past 48 years, i.e., from 190,775.42 km² (95% Confident interval (CI): [189,891.90 km², 191,658.93 km²]) to 813,228.11 km² (95% CI: [811,945.156 km², 814,511.063 km²]) from 1972 to 2019. In the past 48 years, the global average annual expansion rate of ISA is 3.13% (95% CI: [3.12%, 3.15%]), among which Asia is the largest (4.24%), followed by Africa (4.07%), and Europe (2.62%) and North America (2.04%), in sequence. Figure 2 demonstrates the spatial pattern of ISA expansion from 1972 (Figure 2a) to 2019 (Figure 2b). In 1972, ISA was mainly distributed in North America (35.74%, 95% CI: [35.58%, 35.91%]), Europe (27.46%, 95% CI: [27.32%, 28.58%]) and Asia (26.16%, 95% CI: [26.04%, 26.28%]). Europe exceeded North America in

1984, and was overtaken by Asia in 1988 (30.97%, 95% CI: [30.90%, 31.04%]). In general, except for Asia and Africa, the ISA expansion in other continents gradually slowed down since 1990s.

Observing the long time-series dynamics, GISA dataset is generally consistent to the existing global products (Figure 3). Although GHSL provides the ISA map in 1970s, it contains only five cross-section records (1975, 1990, 2000, 2014, and 2018), which seems not sufficient to continuously monitor ISA dynamics during the past half century. On the other hand, GAIA and GAUD provide annual ISA maps from 1985, but their ISAs are underestimated to some extent before 1990s, owing to the data missing of Landsat archives in the early periods (Appendix Figure S1). In contrast, our GISA dataset provides two ISA maps during 1972 and 1984 (Appendix Figure S1), which can be used to fill the gaps of products in 1980s by the spatio-temporal post-processing method. Taking Xi'an (a Chinese major city, Appendix Figure S4) as an example, as there is lack of observation data in East Asia from 1985 to 1987 (Appendix Figure S1), the ISA of Xi'an during this period is unavailable in GAIA and GAUD, but can be delineated by GISA by courtesy of the gap filling algorithm. As shown in Figure 3, at the global scale, the ISA area derived from GISA is slightly larger than that from GAIA and GAUD. A possible reason is that the ISA extent of GAIA and GAUD were constrained by a predefined urban mask (Gong et al., 2020; Liu et al., 2020), but GISA does not have such limitation since it extracted ISA from the whole global land area. Moreover, only GAIA

Table 2 Comparison among existing fine-resolution (30 m) global ISA products, where accuracy was assessed on the random validation points of 54 global cities in 1990 and 2015 which were manually interpreted using Google™ Earth and Landsat images

Year	Region	Metric	GHSL	GAIA	GAUD	GISA
1990	Urban	F-score	0.7989	0.7636	0.8646	0.9274
		Size (10 ⁵ km ²)	2.0277	1.3364	1.6688	2.0149
	Rural	F-score	0.8923	0.8074	0.8949	0.9299
		Size (10 ⁵ km ²)	3.2913	1.9513	2.0974	2.3294
2015	Urban	F-score	0.9527	0.9372	0.9696	0.9882
		Size (10 ⁵ km ²)	2.6305	2.7033	2.5606	2.7477
	Rural	F-score	0.9573	0.9699	0.9878	0.9913
		Size (10 ⁵ km ²)	5.1182	4.6907	4.1050	4.7887

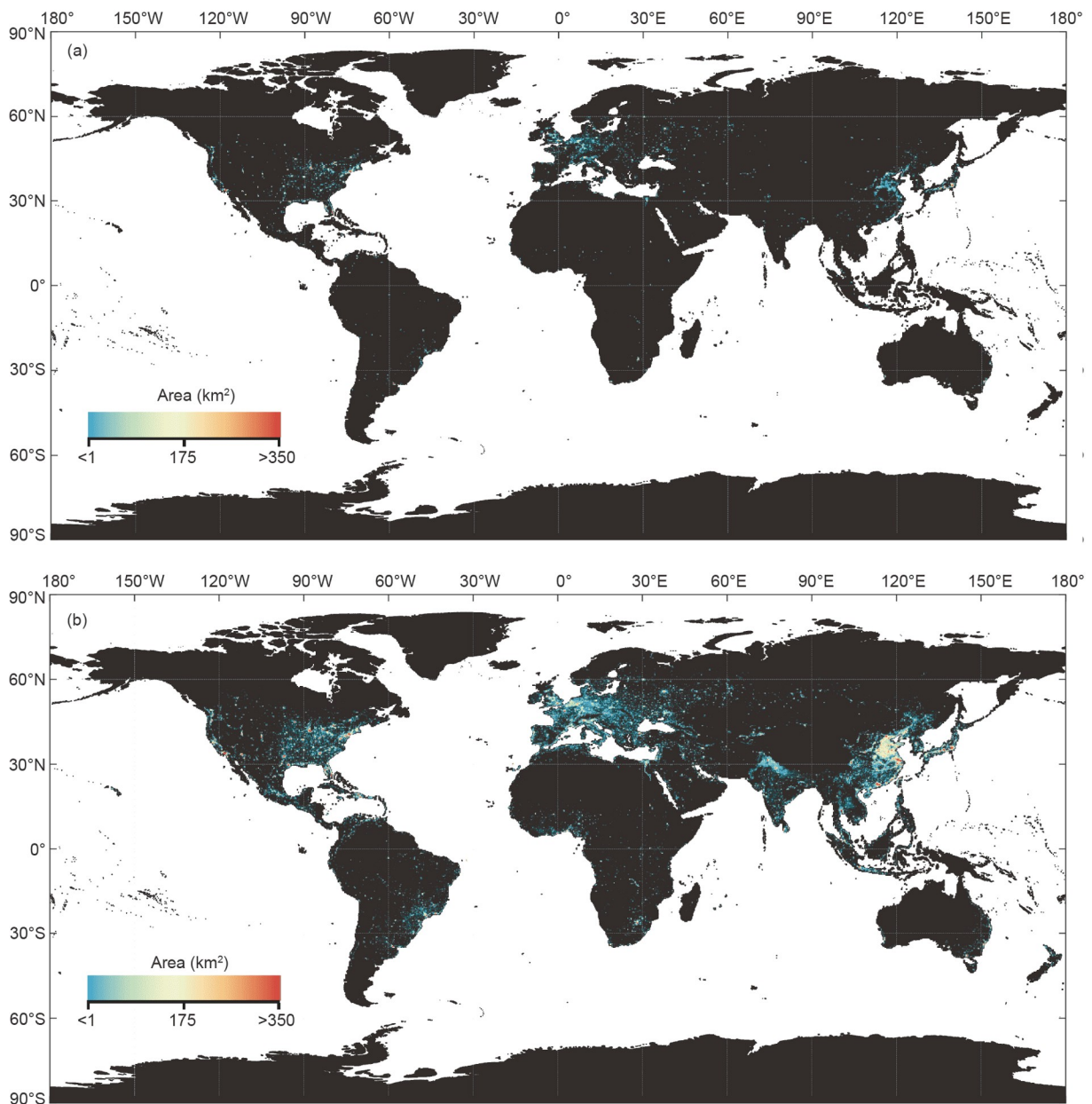


Figure 2 The spatial pattern of ISA in 1972 (a) and 2019 (b). Each pixel indicates the impervious area within the 0.3°×0.3° spatial extent.

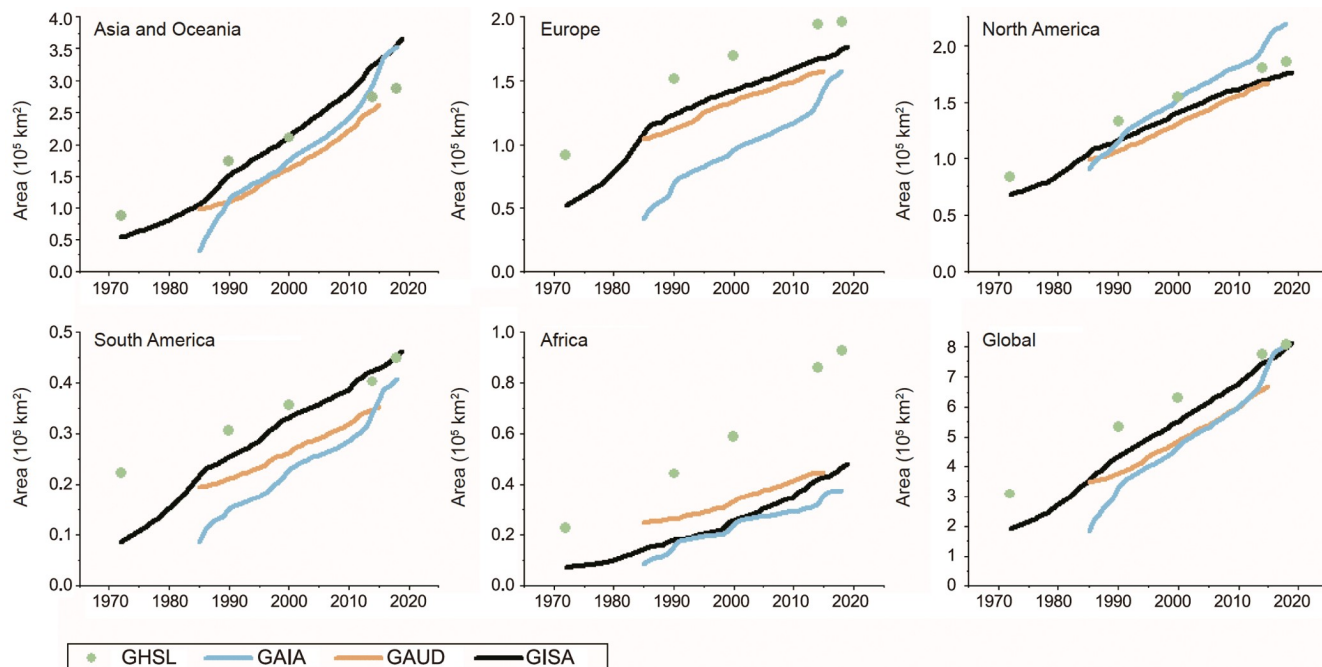


Figure 3 Comparison of ISA expansion among existing fine-resolution (30 m) global products at the continental and global scale. Australia and Oceania are combined with Asia. GHSL, global human settlement layer; GAIA, global artificial impervious areas; GAUD, global annual urban dynamics; GISA, global impervious surface areas.

and GISA continued to monitor ISA dynamics after 2016, and only GISA provides the newest global ISA map in 2019. In addition, based on the third-party validation sets, i.e., GRUMP settlement points (Figure 4) and ZY-3 high-resolution built-up product (Table 1), GISA is superior to GAIA and GAUD. In terms of the random validation points from 270 global cities, the overall accuracy of GISA is also better (Table 1).

The missing of Landsat archives (especially in the early stages) can influence the applicability and reliability of the long time-series ISA products. In general, the valid observations of Landsat gradually become more, and from 1999 the annual global land surface can be covered sufficiently (Appendix Figure S1). Appendix Figure S3 shows the data missing rate (DR) and product missing rate (PR) of GISA. DR or PR in a certain period indicates the area percentage of missing Landsat data or missing mapping results compared to the global ISA extent in 2019, respectively. As seen in Appendix Figure S3, there was a large amount of data absence during 1985 and 1989, most of which appeared in Asia, Australia, and Africa (Appendix Figure S1). Worse, some areas, such as Siberia and the Gulf of Guinea, had very scarce Landsat observations before 1999 (Appendix Figure S1). To deal with this issue, GISA dataset provides two early global ISA maps (i.e., 1972–1977 and 1978–1984) based on the multi-year Landsat image composition. Therefore, the information missing of the ISA product in the early stages (e.g., before 1999) can be effectively addressed by the proposed gap filling and spatio-temporal post-processing algo-

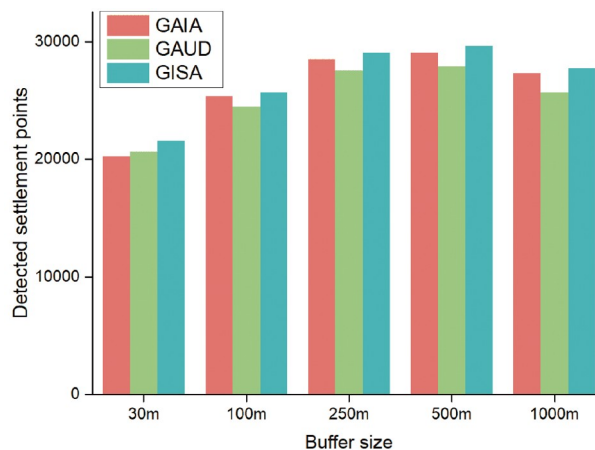


Figure 4 Comparison of detected settlement points between the existing global 30 m ISA products. More detections of the settlement points signify better mapping accuracy.

gorithms. Appendix Figure S3 shows that the PR of GISA is significantly lower than its DR. Notably, some validation points from the 270 cities were located in the areas without valid observations, and hence, after the post-processing, the F-score of GISA was increased from 0.92 to 0.95 after the missing data were effectively filled.

3.2 Global urban expansion pattern

Since 1986, we calculated the proportion of urban expansion types of each continent for every two years (Figure 5). To

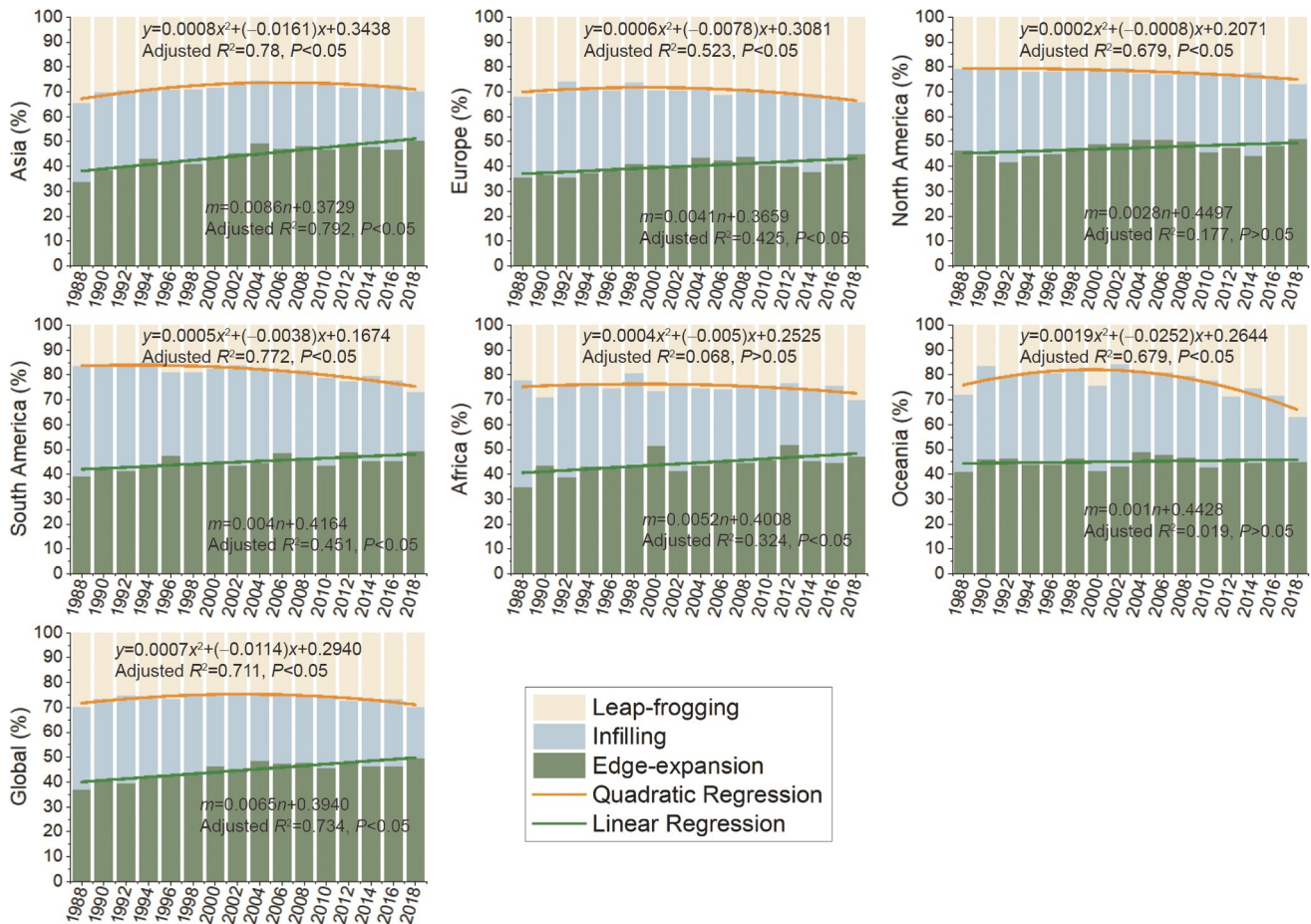


Figure 5 Urban expansion patterns at continental and global scales.

further analyze the patterns of different countries, we list the top ten countries in a descending order in terms of the proportion of each expansion pattern (Appendix Table S2).

On a global scale, edge expansion is the primary pattern in the recent 30 years. Except for Oceania (with non-significant increase) and North America (with fluctuations after 2008), the proportions of edge expansion in most continents show linear growth, indicating that urban sprawl (i.e., edge expansion) is widespread and accelerating. On the whole, the proportion of edge-expansion in North America is highest, possibly owing to the low density urban sprawl happened in this region (Bae and Richardson, 2017). From the temporal perspective, Africa and Asia not only have the fastest urbanization speed in recent decades (United Nations, 2018), but are the major areas with accelerated urban sprawl (Figure 5). Taking two representative countries in Asia, Cambodia and Laos, as examples (Appendix Table S2), in the past 30 years, these two low-income countries have reached low-middle income level, and the economic development is accompanied with rapid expansion of the built-up area along the main

traffic roads, leading to the increasing housing demand for the fast-growing urban residents. However, as the local governments rely heavily on the land finance as their revenue, the fast-rising land prices prevent the inner-urban development, and aggravate the peri-urbanization in a rapid pace (Figure 6a and 6b). At the same time, a number of African countries are also included in the top ten edge-expansion countries (Appendix Table S2). Compared with the European, American and Asian metropolis that are gradually transitioned to smart growth, the growth of African cities is still dominated by accelerated extensive expansion (Figure 6c–6e) (Xu et al., 2019a).

Generally, Eurasia and Oceania have the largest proportions for leapfrogging, which fall and then rise, showing a U-shape (Figure 5). The leapfrogging expansion is derived from two sources: (1) the transformation from rural settlements to urban built-up, and (2) the construction of new towns and urban organic decentralization¹⁾. In the past three decades, the primary driving force of urbanization in Asia was the massive population migration from rural to urban areas. The

1) Organic decentralization refers to the construction of semi-independent towns near large cities which have some urban functions in order to control the expansion of the large cities.

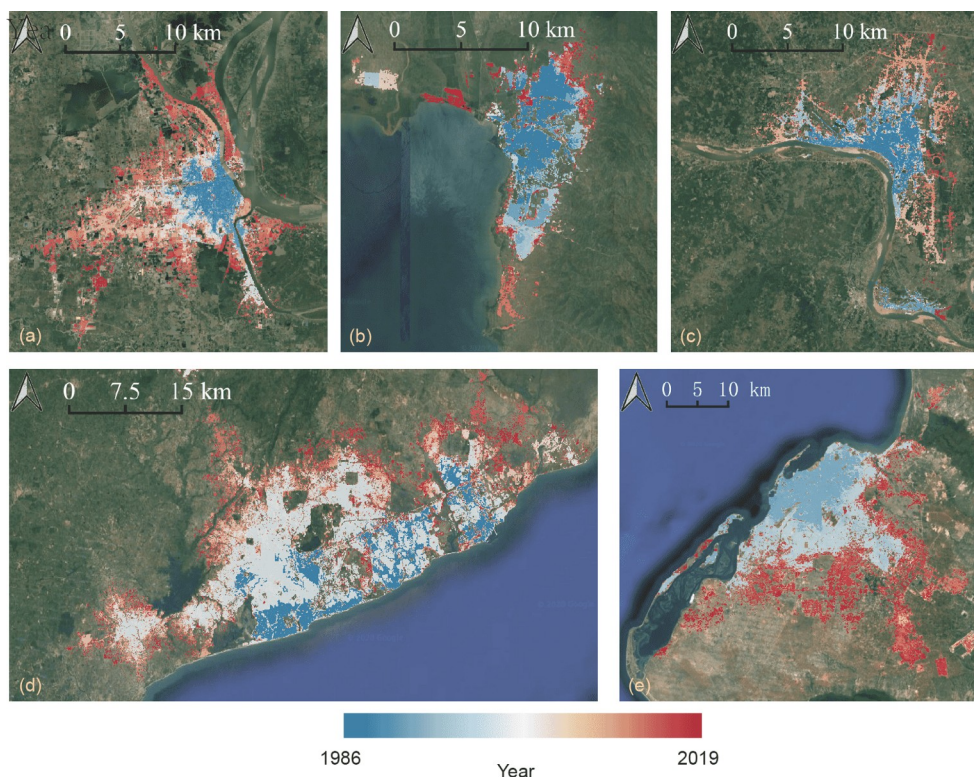


Figure 6 Urban expansion process of typical large cities in Asia and Africa. (a) Phnom Penh, capital of Cambodia, (b) Vientiane, capital of Laos, (c) Accra, capital of Ghana, (d) Bujumbura, capital of Burundi, and (e) Benguela, capital of Angola. In each sub-figure, the true-color remote sensing image is overlaid with urban ISA.

land construction enlarged the urban extent, with a lot of rural land incorporated into the urban areas. For instance, Turkmenistan has the largest proportion of leapfrogging (38.16%, see Appendix Table S2), and [Figure 7a](#) presents the urban expansion process in Ashgabat (capital of Turkmenistan) as well as its adjacent Alha state. As seen from these figures, most of the leapfrogging parcels are derived from the transformation from rural settlements to urban areas (e.g., [Figure 7b](#) and [7c](#)), with a small amount of infrastructure construction around the rural areas (e.g., [Figure 7d](#)). On the other hand, in Europe and Oceania, the major sources of leapfrogging parcels are different from Asia. By the 1980s, the urbanization level in most European and Oceanian countries was stably high. For historical reasons, e.g., the city-state system, a large number of Europe and Oceania cities are with small and medium sizes and compact pattern. For many European large cities, a large amount of green open space was constructed around the urban areas (e.g., the Metropolitan Green Belt ([Mace et al., 2016](#))) to prevent the expansion of urban extent. At the same time, urban decentralization and New Town construction were promoted to mitigate the burden of intra-urban redevelopment, and achieve the harmonious development between old and new urban regions. Thus, the urban development in Europe and

Oceania presented a large proportion of leapfrogging expansion during the past three decades. For instance, Finland, a representative country with the leapfrogging expansion pattern, is one of the earliest countries that practiced the organic decentralization (see Appendix Table S2, and [Figure 7e](#), respectively).

The proportion of infilling expansion pattern gradually decreases from a global perspective, in spite of several fluctuations in Europe and North America ([Figure 5](#)). When a city develops to a certain degree, its urban land supply becomes saturated, and this city will necessarily enter the stage of redevelopment, in order to integrate, renew and reallocate urban resources. Thus, infilling parcels mainly appear in highly urbanized countries (e.g., Japan in Appendix Table S2), or countries with high urban primacy²⁾ (e.g., Nepal in Appendix Table S2). For instance, from 1950s to 1970s, in Japan, the population, economic activities and urban functions were aggregated to Tokyo, Osaka and Nagoya megalopolitan areas, forming the phenomenon of “over dense” in megalopolis and “too sparse” in rural areas ([Figure 8](#)). Therefore, in recent years, a series of regulations (e.g., setting rigid urban boundary) on urban development and construction have been formulated by the Japanese government to limit the over-expansion, control the urban size, and

2) Urban primacy indicates to what extent development is concentrated in a few cities (population, economic activities, services, etc.) in a country.

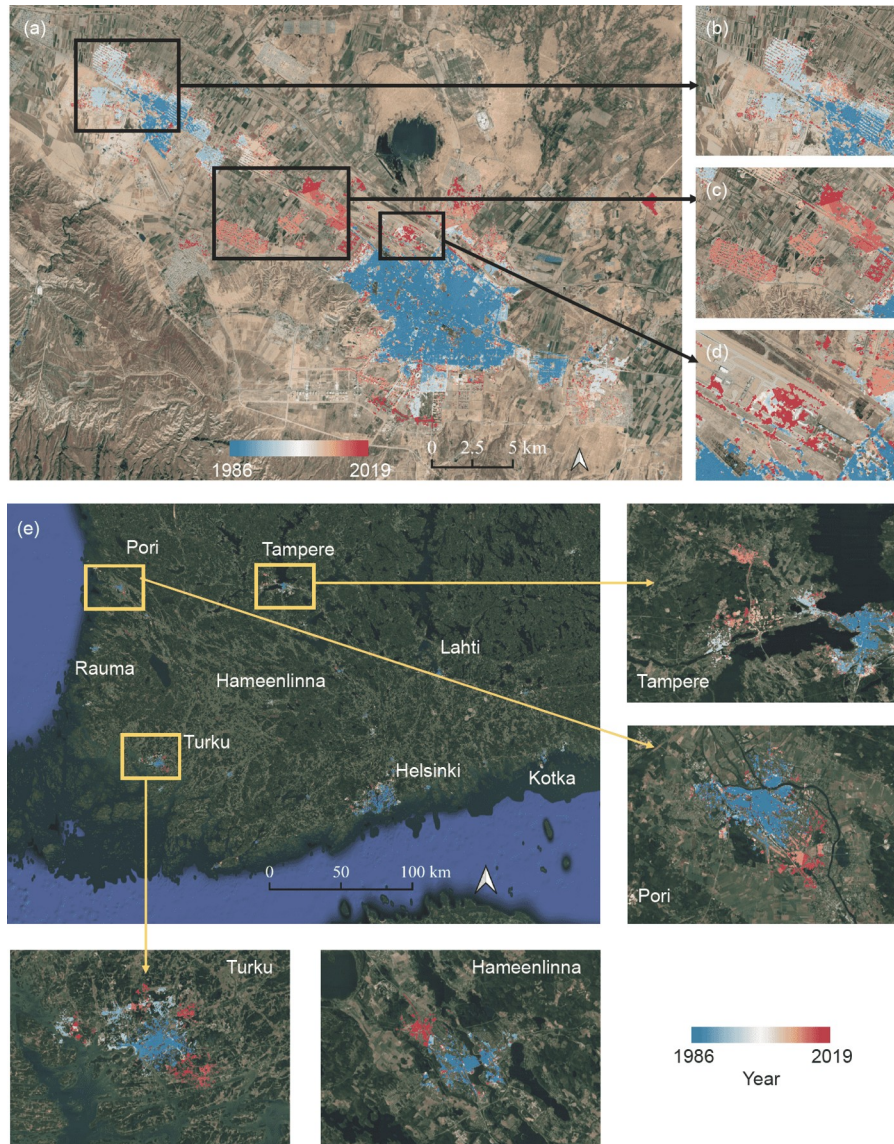


Figure 7 Urban expansion process in Ashgabat and its adjacent Alha state (a) and Southern Finland (e). (b) and (c) zoom-in images: the rural ISA incorporated into urban in recent years; (d) zoom-in image: the infrastructure (i.e., airport) construction around the urban core.

increase land value. Thus, urban renewal and infilling become the primary type of Japan urban land development. Taking another instance, owing to the high urban primacy of Nepal, the spatial expansion pattern of this country is mainly represented by its Capital City, Kathmandu. As seen in Figure 9a, as surrounded by mountains, the space for external expansion of Kathmandu is limited, and hence, the massive old city redevelopment and infilling development led to destruction of ancient buildings and construction of crowded new built-up areas (Figure 9b and 9c). Likewise, many Latin American countries (listed as typical infilling countries in Appendix Table S2) were also characterized by high urbanization level and high urban primacy (Atienza and Aroca, 2013), and hence presented considerable infilling parcels in recent 30 years.

4. Conclusion

Using 30, 872, 69 Landsat images, this research generated the first global impervious surface area (GISA) product from 1972 to 2019. Furthermore, on the basis of GISA, we also produced the first global urban expansion pattern (GUEP) dataset. These new global products are essential for our further understanding on human's utilization and alteration to the natural environments during the past half century.

Compared with the existing global ISA products, although their overall trend is consistent, to some degree, they are distinct in delineating ISA dynamics at the regional or global scale, which is possibly attributed to their different definitions, data sources, methods and samples. Moreover, it should be kept in mind that it is extremely challenging to

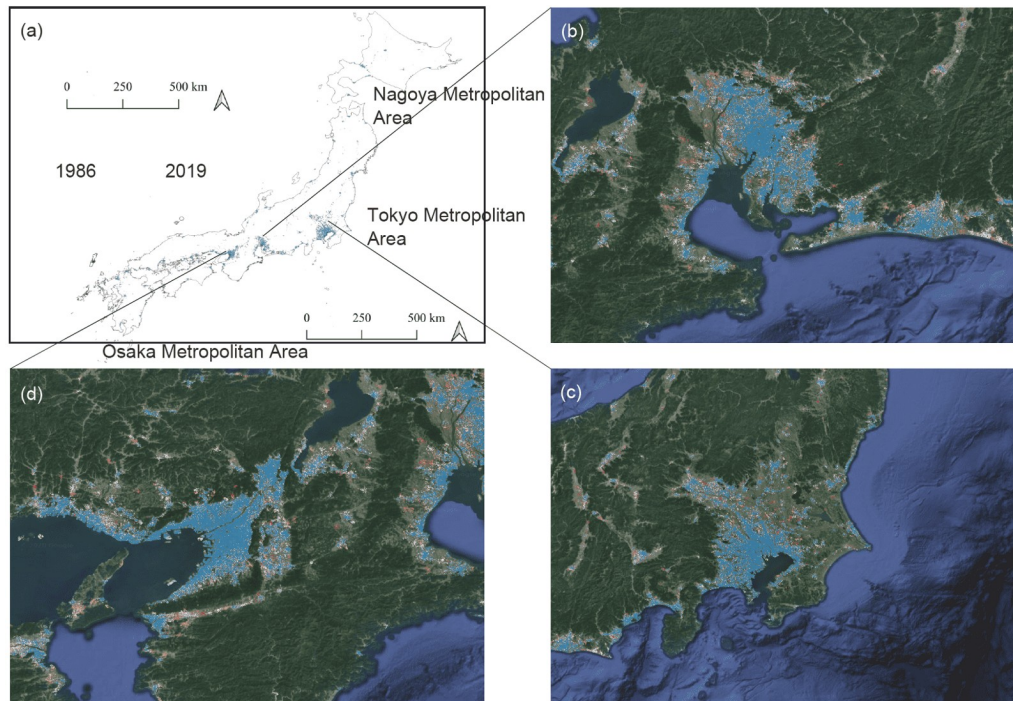


Figure 8 Urban expansion process in Japan (a) and the top three metropolitan areas ((b)–(d)).

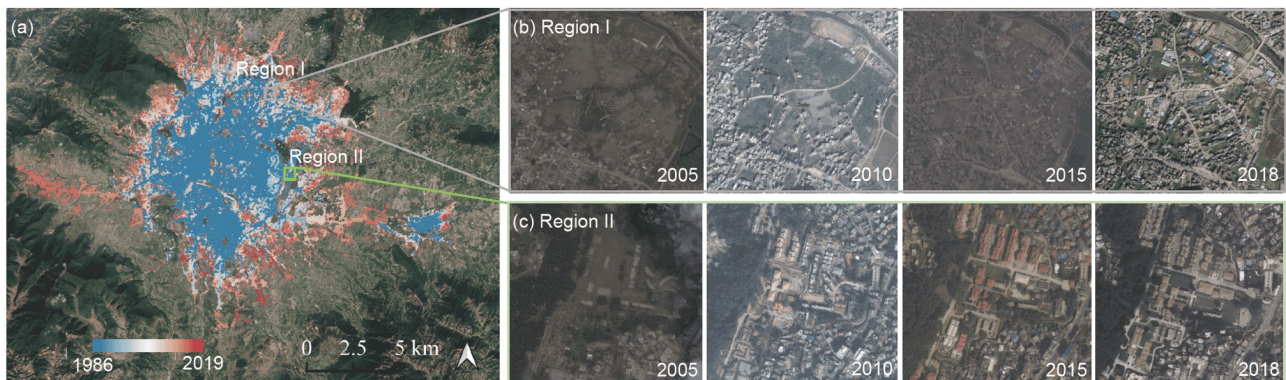


Figure 9 (a) Urban expansion process in Kathmandu valley during 1990–2018. Please note that 1990 is the start year of Landsat observations for this area. The zoom-in very high spatial resolution Google Earth images for the local Region Ib and Region IIc, were taken every five years since 2005.

map the global ISA with a fine spatial resolution and long time-series. Objectively, each product has both pros and cons in different regions and periods. In this regard, more third-party validation sets are imperative to conduct a comprehensive assessment on the existing products. Meanwhile, integration and optimization of existing products deserve further research, in order to advance and clarify our knowledge on the global ISA dynamics gradually. After a century of rapid development, cities all over the world are in different urbanization stages, and, in such context, our GUEP dataset provides a comprehensive, timely, spatial-temporal continuous data for monitoring global urban expansion in recent 30 years. The two global products can be freely download from <http://irsip.whu.edu.cn/resources/dataweb.php>.

Acknowledgements *This work was supported by the National Natural Science Foundation of China (Grant Nos. 42071311, 41771360 & 41971295).*

References

- Atienza M, Aroca P. 2013. Concentration and growth in Latin American countries. In: Cuadrado-Roura J R, Aroca P, eds. *Regional Problems and Policies in Latin America. Advances in Spatial Science (The Regional Science Series)*. Berlin, Heidelberg: Springer. 113–133
- Bae C H C, Richardson H W. 2017. *Urban sprawl in Western Europe and the United States*. London: Routledge. 344
- Balk D L, Deichmann U, Yetman G, Pozzi F, Hay S I, Nelson A. 2006. Determining global population distribution: Methods, applications and data. *Adv Parasit*, 62: 119–156
- Bartholomé E, Belward A S. 2005. GLC2000: A new approach to global land cover mapping from Earth observation data. *Int J Remote Sens*, 26: 1959–1977

- Bicheron P, Leroy M, Brockmann C, Krämer U, Miras B, Huc M, Niño F, Defourny P, Vancutsem C, Arino O, Ranera F, Petit D, Amberg V, Berthelot B, Gross D. 2006. Globcover: A 300 m global land cover product for 2005 using ENVISAT MERIS time series. In: *Proceeding of the Second International Symposium on Recent Advances in Quantitative Remote Sensing*. 538–542
- Bontemps S, Defourny P, Van-Bogaert E, Arino O, Kalogirou V, Perez J R. 2011. GLOBCOVER 2009-Products description and validation report. Technical Report. Paris: UCLouvain and ESA
- Camagni R, Gibelli M C, Rigamonti P. 2002. Urban mobility and urban form: The social and environmental costs of different patterns of urban expansion. *Ecol Econ*, 40: 199–216
- Campbell, Chan L, Custot J, Elmqvist T, Agbemanya R, Alfsen C, Allsopp N, Anderson P, Andersson E, Anh D, Barbe A, Barbosa O, Bernal J, Birch S, Boone R, Combes B, Cooper H, Dogsé P, Zhang R. 2012. *Cities and Biodiversity Outlook-Action and Policy: A Global Assessment of the Links between Urbanization, Biodiversity, and Ecosystem Services*
- Corbane C, Sabo F, Politis P, Syrris V. 2020. GHS-BUILT-S2 R2020A-GHS built-up grid derived from Sentinel-2 global image composite for reference year 2018 using Convolutional Neural Networks (GHS-S2Net). Technical Report. European Commission, Joint Research Centre (JRC)
- ESA. 2017. Land cover CCI product user guide version 2. ESA Libin, Belgium
- Esch T, Heldens W, Hirner A, Keil M, Marconcini M, Roth A, Zeidler J, Dech S, Strano E. 2017. Breaking new ground in mapping human settlements from space—The Global Urban Footprint. *ISPRS J Photogramm Remote Sens*, 134: 30–42
- Gong P, Li X, Wang J, Bai Y, Chen B, Hu T, Liu X, Xu B, Yang J, Zhang W, Zhou Y. 2020. Annual maps of global artificial impervious area (GAIA) between 1985 and 2018. *Remote Sens Environ*, 236: 111510
- Gong P, Li X, Zhang W. 2019. 40-Year (1978–2017) human settlement changes in China reflected by impervious surfaces from satellite remote sensing. *Sci Bull*, 64: 756–763
- Huang X, Xia J, Xiao R, He T. 2019. Urban expansion patterns of 291 Chinese cities, 1990–2015. *Int J Digital Earth*, 12: 62–77
- IPCC. 2016. Report of the Forty-third Session of the IPCC. Nairobi, Kenya, 11–13 April 2016. Technical Report. https://www.ipcc.ch/site/assets/uploads/2018/05/final_report_p43.pdf
- Krayenhoff E S, Moustauoui M, Broadbent A M, Gupta V, Georgescu M. 2018. Diurnal interaction between urban expansion, climate change and adaptation in US cities. *Nat Clim Change*, 8: 1097–1103
- Kuang W. 2019. Mapping global impervious surface area and green space within urban environments. *Sci China Earth Sci*, 62: 1591–1606
- Latham J, Cumani R, Rosati I, Bloise M. 2014. Global land cover share (GLC-SHARE) database beta-release version 1.0-2014. Technical Report. Rome: FAO
- Li X, Zhou Y, Zhu Z, Cao W. 2020. A national dataset of 30 m annual urban extent dynamics (1985–2015) in the conterminous United States. *Earth Syst Sci Data*, 12: 357–371
- Liu C, Huang X, Zhu Z, Chen H, Tang X, Gong J. 2019a. Automatic extraction of built-up area from ZY3 multi-view satellite imagery: Analysis of 45 global cities. *Remote Sens Environ*, 226: 51–73
- Liu C, Zhang Q, Luo H, Qi S, Tao S, Xu H, Yao Y. 2019b. An efficient approach to capture continuous impervious surface dynamics using spatial-temporal rules and dense Landsat time series stacks. *Remote Sens Environ*, 229: 114–132
- Liu X, Huang Y, Xu X, Li X, Li X, Ciaisi P, Lin P, Gong K, Ziegler A D, Chen A, Gong P, Chen J, Hu G, Chen Y, Wang S, Wu Q, Huang K, Estes L, Zeng Z. 2020. High-spatiotemporal-resolution mapping of global urban change from 1985 to 2015. *Nat Sustain*, 3: 564–570
- Mace A, Blanc F, Gordon I R, Scanlon K. 2016. A 21st century metropolitan green belt. Technical Report. London: The London School of Economics and Political Science
- Mbow H O P, Reisinger A, Canadell J, O'Brien P. 2017. Special Report on climate change, desertification, land degradation, sustainable land management, food security, and greenhouse gas fluxes in terrestrial ecosystems (SR2). Technical Report. Geneva, IPCC
- United Nations. 2018. 2018 Revision of World Urbanization Prospects. Technical Report. <https://www.un.org/development/desa/publications/2018-revision-of-world-urbanization-prospects.html>
- Olofsson P, Foody G M, Herold M, Stehman S V, Woodcock C E, Wulder M A. 2014. Good practices for estimating area and assessing accuracy of land change. *Remote Sens Environ*, 148: 42–57
- Pesaresi M, Ehrlich D, Florczyk A J, Freire S, Julea A, Kemper T, Soille P, Syrris V. 2015. GHS built-up grid, derived from Landsat, multitemporal (1975, 1990, 2000, 2014). Technical Report. European Commission, Joint Research Centre, JRC Data Catalogue
- Ran Y H, Li X. 2015. First comprehensive fine-resolution global land cover map in the world from China—Comments on global land cover map at 30-m resolution. *Sci China Earth Sci*, 58: 1677–1678
- Reba M, Seto K C. 2020. A systematic review and assessment of algorithms to detect, characterize, and monitor urban land change. *Remote Sens Environ*, 242: 111739
- Schneider A. 2012. Monitoring land cover change in urban and peri-urban areas using dense time stacks of Landsat satellite data and a data mining approach. *Remote Sens Environ*, 124: 689–704
- Schneider A, Mertes C M. 2014. Expansion and growth in Chinese cities, 1978–2010. *Environ Res Lett*, 9: 024008
- Seto K C, Dhakal S, Bigio A, Blanco H, Delgado G C, Dewar D, Huang L, Inaba A, Kansal A, Lwasa S, McMahon J E, Müller D B, Murakami J, Nagendra H, Ramaswami A. 2014. Chapter 12—Human settlements, infrastructure and spatial planning. In: Edenhofer O, Pichs-Madruga R, Sokona Y, Farahani E, Kadner S, Seyboth K, Adler A, Baum I, Brunner S, Eickemeier P, Kriemann B, Savolainen J, Schlömer S, von-Stechow C, Zwickel T, Minx J C, eds. *Climate Change 2014: Mitigation of Climate Change*. IPCC Working Group III Contribution to AR5. Cambridge: Cambridge University Press
- Seto K C, Güneralp B, Hutyra L R. 2012. Global forecasts of urban expansion to 2030 and direct impacts on biodiversity and carbon pools. *Proc Natl Acad Sci USA*, 109: 16083–16088
- Sulla-Menashe D, Gray J M, Abercrombie S P, Friedl M A. 2019. Hierarchical mapping of annual global land cover 2001 to present: The MODIS Collection 6 Land Cover product. *Remote Sens Environ*, 222: 183–194
- Weng Q. 2001. Modeling urban growth effects on surface runoff with the integration of remote sensing and GIS. *Environ Manage*, 28: 737–748
- Wulder M A, White J C, Loveland T R, Woodcock C E, Belward A S, Cohen W B, Fosnight E A, Shaw J, Masek J G, Roy D P. 2016. The global Landsat archive: Status, consolidation, and direction. *Remote Sens Environ*, 185: 271–283
- Xu G, Dong T, Cobbinah P B, Jiao L, Sumari N S, Chai B, Liu Y. 2019a. Urban expansion and form changes across African cities with a global outlook: Spatiotemporal analysis of urban land densities. *J Cleaner Production*, 224: 802–810
- Xu G, Jiao L, Liu J, Shi Z, Zeng C, Liu Y. 2019b. Understanding urban expansion combining macro patterns and micro dynamics in three Southeast Asian megacities. *Sci Total Environ*, 660: 375–383
- Xu Y, Yu L, Peng D, Zhao J, Cheng Y, Liu X, Li W, Meng R, Xu X, Gong P. 2020. Annual 30-m land use/land cover maps of China for 1980–2015 from the integration of AVHRR, MODIS and Landsat data using the BFAST algorithm. *Sci China Earth Sci*, 63: 1390–1407
- Yang Y, Xiao P, Feng X, Li H. 2017. Accuracy assessment of seven global land cover datasets over China. *ISPRS J Photogramm Remote Sens*, 125: 156–173
- Zhou D, Zhao S, Liu S, Zhang L, Zhu C. 2014. Surface urban heat island in China's 32 major cities: Spatial patterns and drivers. *Remote Sens Environ*, 152: 51–61